Rapid Surface Large-Change Monitoring by Repeat-Pass GEO SAR Multibaseline Interferometry

Li, Yuanhao; Hu, Cheng; Ao, Dongyang

DOI
10.1109/LGRS.2020.3026326

Publication date
2022

Document Version
Final published version

Published in
IEEE Geoscience and Remote Sensing Letters

Rapid Surface Large-Change Monitoring by Repeat-Pass GEO SAR Multibaseline Interferometry

Yuanhao Li, *Member, IEEE*, Cheng Hu, *Senior Member, IEEE*, and Dongyang Ao

***Abstract*— Fast observations of rapid surface large-changes are demanded in disaster evaluations and scientific studies. Digital elevation model (DEM) differencing before and after the events is an effective way to retrieve the changes. Owing to a short repeat cycle, geosynchronous synthetic aperture radar (GEO SAR) systems can quickly obtain repeat-pass data and generate postevent DEMs by interferometry. However, interferometric baselines under its quick revisit cases are short, resulting in generating low-accuracy postevent DEMs. Moreover, surface large-changes can bring height ambiguity problems under the single-baseline interferometric processing. In this letter, we address the problem through a multibaseline (MB) processing. Since GEO SAR MB data can derive from the repeat-pass interferometric data of different subapertures and revisits, a subaperture-decomposition-based temporal and spatial MB method is proposed. The simulation results verify the effectiveness of the proposed method, where the quickly generated postevent DEM can help to realize the rapid large-elevation change observations.**

***Index Terms*— Change detection, digital elevation model (DEM), geosynchronous synthetic aperture radar (GEO SAR), interferometric SAR.**

I. Introduction

A TIMELY evaluation of rapid surface large-changes is significance in disaster emergency reactions and scientific goals for understanding the Earth surface activities [1], [2]. The preevent and postevent digital elevation model (DEM) differencing is a good way to obtain the surface large-changes, because the synthetic aperture radar (SAR) interferograms in these regions obtained before and after the events have no coherence [3]. However, obtaining an accurate timely postevent DEM is always an issue. Available DEMs from both low Earth orbit (LEO) lasers and SARs could only be accessed after dozens of days due to their long repeat cycles [4]. Meanwhile, airborne platforms do not fit the DEM generation tasks for large-scale scenes and also are limited by the weather conditions.

Manuscript received February 9, 2020; revised June 8, 2020 and September 13, 2020; accepted September 18, 2020. Date of publication October 1, 2020; date of current version December 21, 2021. This work was supported by the National Natural Science Foundation of China under Grant 61960206009. *(Corresponding author: Cheng Hu.)*

Yuanhao Li is with the School of Information and Electronics, Beijing Institute of Technology, Beijing 100081, China, and also with the Department of Geoscience and Remote Sensing, Delft University of Technology, 2628 Delft, The Netherlands (e-mail: lyh.900101@163.com).

Cheng Hu and Dongyang Ao are with the School of Information and Electronics, Beijing Institute of Technology, Beijing 100081, China (e-mail: cchchb@163.com; aodongyang@qq.cm).

Digital Object Identifier 10.1109/LGRS.2020.3026326

In order to monitor rapid surface large-changes promptly, geosynchronous (GEO) SAR will be an effective tool owing to its short repeat cycle (almost one day) and long coverage capability for the targets (dozens of minutes to hours) [5], [6]. By providing repeat-pass SAR interferometry (InSAR) data within two days, it can generate a timely postevent DEM for the dramatic surface change monitoring. However, a long interferometric baseline is required to improve the accuracy of the generated DEM, which needs long revisit intervals [7]; thus, it will be contradicted to the temporal requirement. For example, an interferometric baseline from a ten-day revisit interval can enable a generated DEM accuracy smaller than 10 m at the apogee under a single look case. In addition, large surface changes may produce height ambiguities by introducing phase jumps in the single-baseline InSAR processing. Fortunately, this problem can be addressed by using temporal and spatial multibaseline (MB) data sets of GEO SAR. Spatially, since an integration time of several minutes for a subaperture can achieve its designed moderate resolution, a ten times longer full-aperture can provide many subapertures with varied interferometric baselines [8]. In temporal, we can also acquire a series of MB data from different repeat-passes due to quick revisits of GEO SAR. Therefore, with this method, we can improve the accuracy of the generated postevent DEM and solve the height ambiguity problem by using GEO SAR MB data sets [9].

In this letter, we demonstrate our subaperture-decomposition-based temporal and spatial MB (SAD-TSMB) method to generate postevent DEMs in Section II. The utilized MB data sets from different subapertures and revisit intervals of GEO SAR are explained, and the overall processing procedures are described. In Section III, we provide a detailed analysis of the variation of interferometric baselines from different subapertures and revisits to show the MB capability of GEO SAR. The accurate simulations are conducted to verify our proposed method and the related performance is discussed under different cases. Finally, conclusions are drawn in Section IV.

II. Proposed Method

In this section, we illustrate the proposed GEO InSAR SAD-TSMB method to generate postevent DEMs for rapid surface large-change monitoring. The sketch map of the concept is briefly shown in Fig. 1.

Three decomposed subapertures in the full-aperture and two revisit interval cases are shown in Fig. 1 as an example, where it is assumed that the satellite visits the target region after the event in day 0. Two 1-day repeat InSAR data can

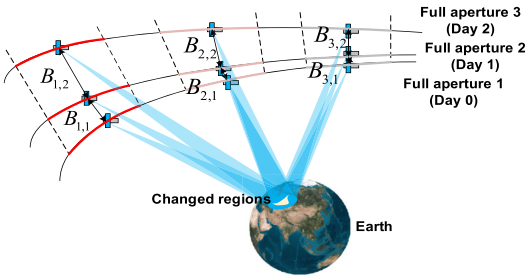

Fig. 1. Sketch map of the SAD-TSMB method in GEO InSAR.

derive from the day 0 image with the day 1 image, and the day 1 image with the day 2 image. The day 0 image and the day 2 image form the two-day repeat data. For each subaperture, we generate the accordingly interferograms of different revisits based on the same way; therefore, we have $N \cdot M(M+1)/2$ interferograms in total, where N is the number of the decomposed subaperture and M stands for the maximum revisit interval of continuous data acquisition. M is selected as a tradeoff between the temporal resolution for the large-change monitoring and the estimation accuracy. A large M can provide more feasible MB data to reduce noises, while it can make the timeliness worse. The entire processing flowchart of the GEO InSAR SAD-TSMB method for rapid large-elevation change monitoring is shown in Fig. 2. The main processing steps include as follows.

A. Subaperture Decomposition and Interferogram Generation

The first step in the SAD-TSMB processing, the subaperture decomposition, is realized by obtaining the number of possible subapertures and calculating the orbit position of the individual subaperture. Before the decomposition, the lengths of the full-aperture and the subaperture should be settled. The full-aperture length is determined by the coverage time of GEO SAR system toward the target, which can be expressed as

$$T_c = \frac{L_c(\mathbf{p}, D, \theta)}{v_b(\mathbf{p}, \theta)} \tag{1}$$

where L_c is the length of the footprint, $\mathbf{p}$ is the vectors of the orbit elements, D is the along-track antenna length, θ is the look angle, and v_b is the beam velocity on the ground.

Meanwhile, the length of the subaperture can be calculated as

$$T_a = \frac{\lambda R(\mathbf{p})}{2v_s(\mathbf{p}) \cdot \rho_a} \tag{2}$$

where λ is the wavelength, R is the slant range, v_s is the satellite velocity, and ρ_a is the azimuth resolution.

After the lengths of the apertures are selected, we can get the maximum number of the possible subapertures by

$$N = \text{int}\left[\frac{T_c - 2T_m + T_a \cdot P}{(1+P) \cdot T_a}\right] \tag{3}$$

where T_m is the margin time at the edges of the full-aperture, P is the percentage of the subaperture length describing the protected window length between adjacent subapertures, and int[·] is the function converting the value into an integer number.

When all the aforementioned information is acquired, the position of each subaperture can be determined and the corresponding interferograms can be generated by the complex conjugation of each GEO InSAR data pair.

B. Temporal MB Processing

Based on the maximum likelihood (ML) estimator, low accuracy DEMs are generated by each subaperture MB InSAR data from different revisit intervals, which are required in the following terrain correction and spatial MB processing. The utilized ML method can improve height estimation accuracy and eliminate the ambiguity. The overall ML likelihood function for each subaperture can be written as [10]

$$F_L\{\mathbf{\Phi}(i,j)|h(i,j)\} = \prod_{n=1}^{M(M+1)/2} f\{\varphi_n(i,j)|h(i,j)\} \tag{4}$$

where φ is the interferometric phase, $\mathbf{\Phi}$ is the temporal MB phase vector, h is the height, i and j are the indices of the pixels, $f\{\cdot\}$ is the probability density function of the wrapped phase in the individual interferogram which relates to coherences γ and interferometric baselines.

The height estimation values based on the ML method can be expressed as

$$\hat{h}_{L,i,j} = \arg\max\{F_L\{\mathbf{\Phi}(i,j)|h(i,j)\}\}, \quad \text{s.t. } \gamma(i,j) > \gamma_{\text{th}} \tag{5}$$

where γ_{th} is the threshold of the coherence. It is applied to remove the low coherence regions at severe layover and shadow areas if possible.

C. Terrain Correction

Terrain correction is applied to remove the geometric distortions produced by the terrain variation in the subaperture interferograms. It is a necessary step to align these interferograms of different viewing angles in GEO InSAR SAD-TSMB processing if a second ML height estimation will be operated. To realize it, the generated DEMs in the previous step are utilized to geocode all the subaperture interferograms. Since temporal MB data is applied to improve the accuracy, these DEMs have better quality than the single-baseline ones and can support the correction. In this way, all the subaperture interferograms are coregistered without geometry distortions after the correction. It should also be noted that when generating each subaperture low-accuracy DEM the geocoding information can be reused in the terrain correction; thus, the required calculation time is reduced.

D. Spatial MB Processing and DEM Differencing

In this step, we consider spatial MB processing by fusing these N subaperture data to improve the accuracy of the generated DEM. Two ways can be implemented.

1) Second ML Height Estimation: When all the subaperture interferograms are coregistered, for each pixel, the temporal and spatial overall ML likelihood functions $F_H\{\cdot\}$ and the height estimation expression $\hat{h}_{H,i,j}$ are written as

$$\begin{cases} F_H\{\mathbf{\Phi}'(i,j)|h(i,j)\} = \prod_{n=1}^{N} F_L\{\mathbf{\Phi}_n(i,j)|h(i,j)\} \\ \hat{h}_{H,i,j} = \arg\max\{F_H\{\mathbf{\Phi}'(i,j)|h(i,j)\}\}, \quad \text{s.t. } \gamma(i,j) > \gamma_{\text{th}} \end{cases} \tag{6}$$

where $\mathbf{\Phi}'$ is the temporal and spatial MB phase vector.

2) DEM Averaging: To decrease the data processing burden, we can also directly generate the high accuracy postevent DEM by averaging all the low accuracy DEMs, which is given

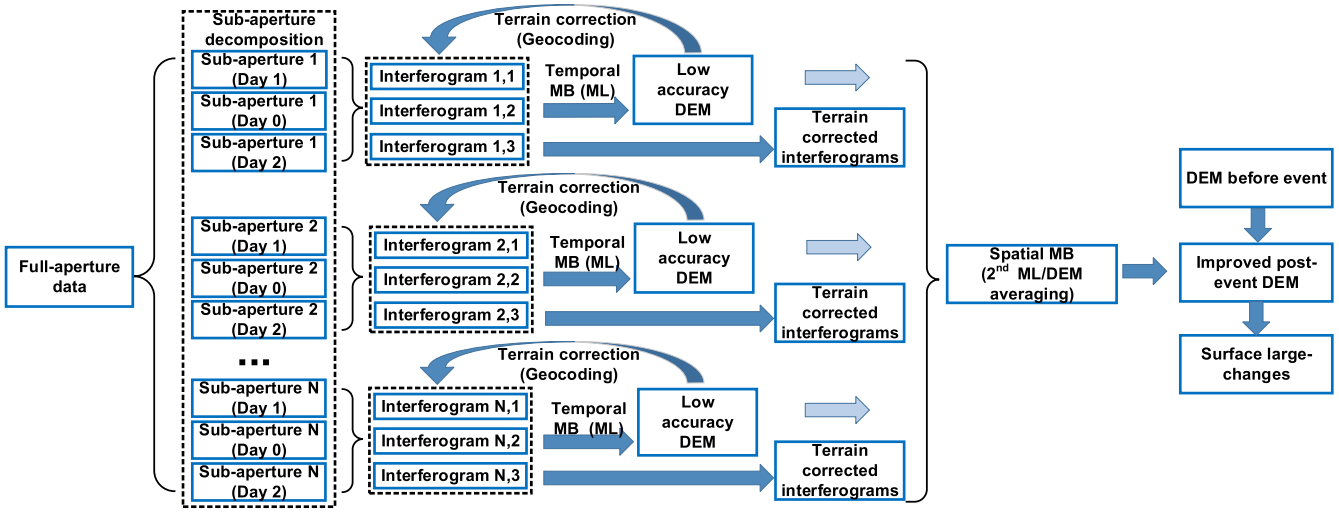

Fig. 2. Flowchart of the GEO InSAR SAD-TSMB method for rapid surface large-change monitoring.

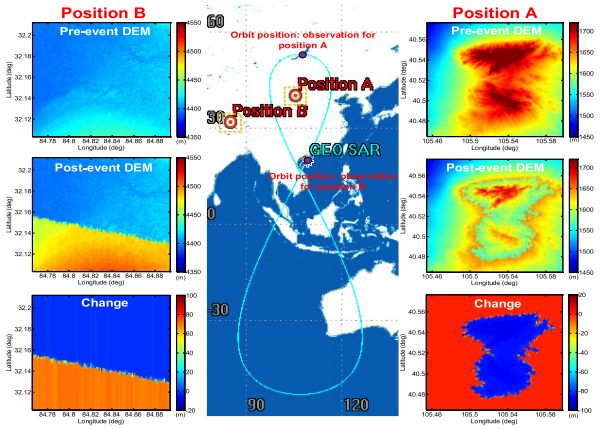

Fig. 3. Nadir-point trajectory of the "large-8" GEO SAR orbit and the observation scenes (positions, preevent DEMs, postevent DEMs, and the changes).

by

$$\hat{h}_{H,i,j} = \frac{1}{N}\sum_{n=1}^{N} \hat{h}_{L,i,j}(n). \tag{7}$$

Finally, the surface large-changes can be simply obtained by the differencing between the generated postevent DEM and the DEM before the event, which is shown as the last step in Fig. 2.

III. Simulation and Performance Discussion

In this section, GEO SAR SAD-TSMB performance is analyzed based on simulations, whose parameters are listed in Table I. The large "figure-8" GEO SAR orbit, as shown in Fig. 3, is utilized as the input orbit. Generally, interferometric baselines of GEO SAR vary obviously for different locations [7]. Observation scenes also include distinguished land topographies. Thus, we consider two scenes observed by different looks angles and orbit positions. One scene is a near apogee observation (Fig. 3 position A), where its baselines are relatively small, and includes many mountains and valleys. As shown in Fig. 3 position B, the other scene is a relatively flat plateau, which is an observation approaching the equator and has large baselines. Their preevent DEMs derive from the shuttle radar topography mission (SRTM) 1 arc-second data set and we assume some surface large changes are generated to produce the postevent DEMs.

TABLE I

Simulation and Processing Parameters. First Pair is the InSAR Pair Generated by the Day 0 and Day 1 Images; Second Pair is the Interferogram Generated by the Day 0 and the Day 2 Data; Third Pair Uses the Data of the Day 1 and the Day 2

Parameter				Case 1	Case 2
Orbit inclination (deg)				53	
Orbit eccentricity (deg)				0.07	
Wavelength (m)				0.24	
Bandwidth (MHz)				18	
Antenna size (m)				30	
Incidence angle (deg)				~14	~28
Integration time (s)				120	
Location of scene center point				(40.53°N, 105.53° E)	(32.16°N, 84.83°E)
Scene size (deg)				0.15	0.15
Observation interval of true anomaly (deg)				[179.4, 184.6]	[234.7, 240.2]
Sub-aperture No.	1	True anomaly (deg)		180.3	235.6
		Height ambiguity (m)	1st pair	491.8	141.5
			2nd pair	310.7	69.9
			3rd pair	843.5	138.2
	2	True anomaly (deg)		181.2	236.5
		Height ambiguity (m)	1st pair	399.7	140.8
			2nd pair	238.4	69.6
			3rd pair	590.3	137.6
	3	True anomaly (deg)		182.0	237.5
		Height ambiguity (m)	1st pair	320.4	140.2
			2nd pair	182.2	69.3
			3rd pair	422.5	137.0
	4	True anomaly (deg)		182.9	238.4
		Height ambiguity (m)	1st pair	273.7	139.8
			2nd pair	151.6	69.1
			3rd pair	339.6	136.5
	5	True anomaly (deg)		183.8	239.3
		Height ambiguity (m)	1st pair	239.4	139.4
			2nd pair	130.1	68.9
			3rd pair	284.8	136.1
SNR (dB)				10	
Temporal decorrelation factor				0.95	
Number of looks				6	25

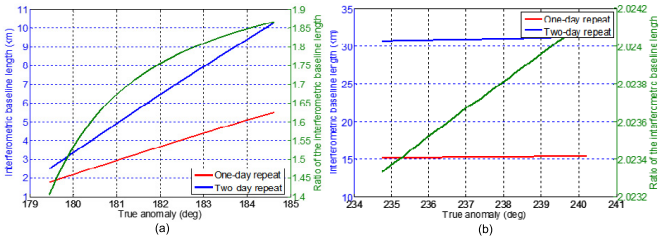

Fig. 4. Interferometric baseline variations within the full-aperture for the one-day repeat and two-day repeat cases (taking the day 0 data as a reference) and their ratios. (a) Case 1 (near the apogee). (b) Case 2 (near the equator).

To verify the MB capability of GEO SAR, interferometric baseline variations within the full-aperture for two cases (one-day and two-day repeats) are shown in Fig. 4. The interferometric baselines of the two revisits are a few kilometers and vary more than twice within the full aperture for case 1 (near the apogee). Meanwhile, their ratio changes from 1.4 to nearly 1.9 within the aperture. In case 2 (near the equator), the two revisit interferometric baselines are much larger than those in case 1, while their lengths and ratio within the aperture vary much smaller. These varied baselines provide the MB capability for both the noise smoothing and the height ambiguity eliminating. Compared to case 2, case 1 has a higher MB capability from a larger baseline diversity. In our simulations, the postevent DEMs are generated after two days of the event to achieve both the timeliness and the baseline diversity (see Fig. 2). Five subapertures are decomposed from the full-aperture. We reserve a 2-min window at the edges of the full-aperture and a margin region of a length of subaperture between different subapertures to decrease the duty cycle of the system or realize the possible working mode shifts. The information of these subapertures and the corresponding height ambiguities are listed in Table I.

When simulating the interferograms of subapertures, the selected DEMs have been resampled into GEO SAR image coordinates based on the orbit positions of the subapertures and the scene geometries to generate topographic phases. We assume the back-projection imaging algorithm is used and the imaging grids are along the latitude and longitude. For other phase components, besides the decorrelation noises generated from the parameters given in Table I, we also consider the impacts of atmospheric phases and orbit error phases. Since atmospheric artifacts can seriously deteriorate the performance of DEM retrievals, some corrections for these phases must be done in the preprocessing. The split-spectrum method is applied to remove ionospheric phases [11]. Tropospheric phases can be compensated based on weather models and multispectral observations [12]. Thus, we consider the residual phases after these corrections in our simulations. Assuming a feasible averaging scale in the split-spectrum processing is 5 km, the simulated residual ionospheric phases have a standard deviation of 0.13 rad and a spatial correlation scale of 5 km. The residual tropospheric phases are considered as uncorrelated noises and have a standard deviation of nearly 0.5 rad at L-band (i.e., corresponding to the correction accuracy of 1 cm for tropospheric delays). We take a 10-cm orbit accuracy in three dimensions into account to generate the orbit error phases in the simulation. Because of the high orbit and small simulated scenes, the incidence angles change less than 0.2° in the scene, which results in a small variation of the orbit error phase in the scene. Fig. 5 shows one realization

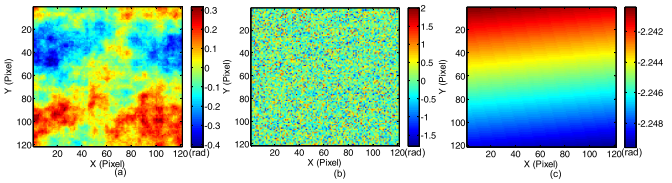

Fig. 5. Simulated residual atmospheric phases after corrections and the orbit phases (one realization). (a) Residual ionospheric phase. (b) Residual tropospheric phase. (c) Orbit error phase.

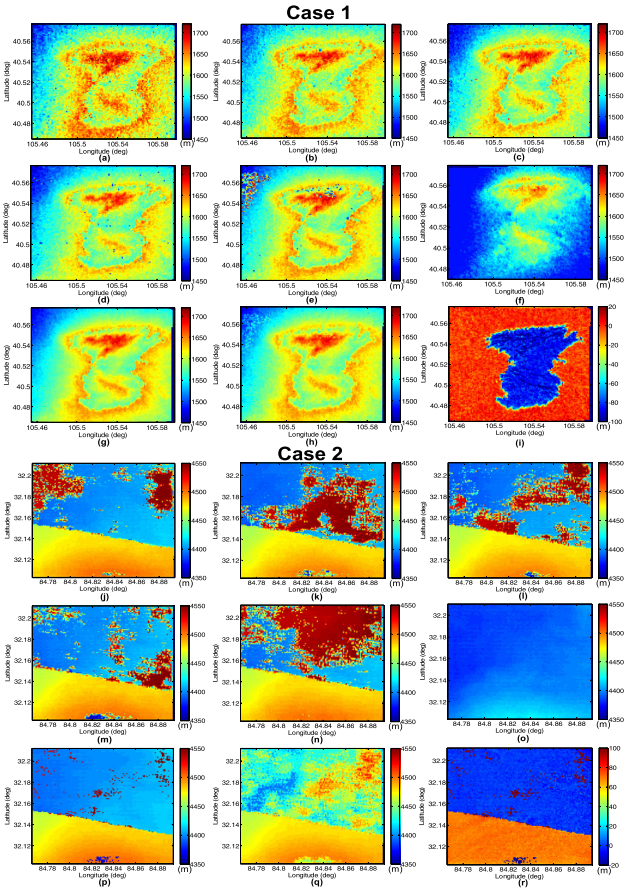

Fig. 6. Generated postevent DEMs and the surface changes. (a)–(e) Case1: Postevent DEM from the single subaperture MB data (No. 1–5). (f) DEM from the signal-baseline data (the fifth subaperture and two-day repeat). (g) DEM from SAD-TSMB (second ML and all the subapertures). (h) DEM from SAD-TSMB (DEM-averaging and all the subapertures). (i) Retrieved surface change by (g). (j)–(n) Case2: Postevent DEM from the single subaperture MB data (No. 1–5). (o) DEM from the signal-baseline data (the fifth subaperture and two-day repeat). (p) DEM from SAD-TSMB (second ML and all the subapertures). (q) DEM from SAD-TSMB (DEM-averaging and all the subapertures). (r) Retrieved surface change by (p).

of the residual atmospheric and orbit error phases. Since the separation between each subaperture is hundreds of kilometers, we treat these phase error sources independently for each interferogram.

After obtaining the interferograms, following Fig. 2, we conduct the SAD-TSMB processing, which also includes the general phase filtering, multilooking, and geocoding. The interferograms have approximately 100 m resolutions in both ground-range and azimuth direction after multilooking. One stable reference point is taken to acquire absolute heights. The generated postevent DEMs by SAD-TSMB are shown in Fig. 6. To compare the results, we also generate the DEMs

TABLE II
PERFORMANCE ANALYSIS OF THE DEMS GENERATED BY DIFFERENT CASE

Data	RMSE of case 1 (m)	RMSE of case 2 (m)
Sub-aperture 1	22.5	50.7
Sub-aperture 2	16.9	64.0
Sub-aperture 3	15.4	53.2
Sub-aperture 4	17.1	41.9
Sub-aperture 5	24.6	76.7
Sub-aperture 5 (Single-baseline)	73.0	50.7
SAD-TSMB (2nd ML)	10.0[1]/10.8[2]/10.4[3]	24.6[1]/34.2[2]/31.3[3]
SAD-TSMB (DEM averaging)	11.7[1]/11.7[2]/12.7[3]	40.2[1]/36.0[2]/45.2[3]

[1] all sub-apertures;
[2] without the sub-aperture with the worst accuracy;
[3] without the sub-aperture with the best accuracy.

from the single-baseline data sets (the two-day repeat data of the fifth subaperture) and the DEMs generated by the MB method from the single subapertures. The corresponding root mean square error (RMSE) analysis is provided in Table II.

From Fig. 6(a)–(f) and Table II, although all the retrieved postevent DEMs from different data sets in case 1 are alike to the reference DEM in Fig. 3, the single baseline DEM has a much larger RMSE error than the subaperture MB DEMs. In case 2, the subaperture MB results shown in Fig. 6(j)–(n) can retrieve the large change, which cannot be distinguished in the single-baseline DEM [Fig. 6(o)]. However, because the large baselines of the subaperture MB data in case 2 give rise to many ambiguity errors (dark red areas), the generated DEMs have low accuracy. When the SAD-TSMB method is applied, as shown in Fig. 6(g), (h), (p), and (q) and Table II, both the accuracies of the generated DEMs in two cases improve and the height ambiguities are effectively addressed. It can also be concluded that the second ML-based SAD-TSMB method achieves better results than the DEM averaging because it has minimal RMSEs in both two cases (i.e., 10 and 24.6 m, respectively). Its good performance profits from more accurate overall likelihood functions in the final height estimation by fusing the coherence-weighted likelihood functions from all subapertures. In this way, it can effectively reduce noises and ambiguity errors. The performance of the DEM-averaging SAD-TSMB depends much on the quality of individual subaperture MB DEM. In case 1, because of the relatively small RMSE of the individual DEM, these averaged DEMs are much accurate than the single-baseline DEM. On the contrary, averaging the DEMs with many ambiguity errors in case 2 does not help to improve the accuracy much. Meanwhile, although more subapertures improve the performance of the second ML-based SAD-TSMB, low-accuracy subapertures have little benefit for the DEM averaging method and even make the averaging performance worse. Comparing two studied cases, the method performs better in case 1 with higher robustness to noises and ambiguity errors, because of both the better baseline diversity and lengths in its MB data from the near apogee observation. Without a good baseline composition, case 2 still suffers some residual ambiguity errors, which ends up with a higher RMSE.

According to the generated postevent DEMs of the second ML-based SAD-TSMB, we can finally obtain the surface changes by the DEM differencing with the preevent DEMs. They are shown in Fig. 6(i) and (r) under two cases, which are similar to the reference produced changes shown in Fig. 3. These results verify that the postevent DEM generation for the rapid surface large-change monitoring can benefit from the proposed SAD-TSMB method.

IV. CONCLUSION

Aiming at rapid surface large-change monitoring by DEM differencing, this letter has proposed a SAD-TSMB algorithm by using GEO SARs to generate postevent DEMs and has presented its performance. GEO InSAR data of long observation times and quick revisits provides the required temporal and spatial MB data. We have conducted the simulations of two scenes observed by the typical orbit positions of GEO SAR to verify the method, which suggests the generated postevent DEM under the short-revisit case has an improved accuracy for large-change observations. The results show that the second ML-based SAD-TSMB algorithm performs well for both two cases. The SAD-TSMB processing through the DEM averaging relies much on the high-quality subaperture MB data; without them, averaging many poor DEMs does not help to improve the accuracy. The near apogee observations can provide a better MB capability for SAD-TSMB processing due to their good diversities and proper lengths of the baselines. Thus, according to different locations of target regions, proper observations for the processing should be achieved by adjusting incidence angles and squint angles, which will be deeply studied in the future.

REFERENCES

[1] W. Zheng, M. E. Pritchard, M. J. Willis, and L. A. Stearns, "The possible transition from glacial surge to ice stream on vavilov ice cap," *Geophys. Res. Lett.*, vol. 46, no. 23, pp. 13892–13902, Dec. 2019.
[2] Y. Gao, "Investigation and dynamic analysis of the long runout catastrophic landslide at the Shenzhen landfill," *Environ. Earth Sci.*, vol. 76, no. 1, p. 13, Dec. 2017.
[3] T. Wang, S. Jonsson, and R. F. Hanssen, "Improved SAR image coregistration using pixel-offset series," *IEEE Geosci. Remote Sens. Lett.*, vol. 11, no. 9, pp. 1465–1469, Sep. 2014.
[4] G. Krieger *et al.*, "TanDEM-X: A satellite formation for high-resolution SAR interferometry," *IEEE Trans. Geosci. Remote Sens.*, vol. 45, no. 11, pp. 3317–3341, Nov. 2007.
[5] J. Ruiz-Rodon, A. Broquetas, E. Makhoul, A. M. Guarnieri, and F. Rocca, "Nearly zero inclination geosynchronous SAR mission analysis with long integration time for Earth observation," *IEEE Trans. Geosci. Remote Sens.*, vol. 52, no. 10, pp. 6379–6391, Oct. 2014.
[6] Y. Li, D. Ao, C. O. Dumitru, C. Hu, and M. Datcu, "Super-resolution of geosynchronous synthetic aperture radar images using dialectical GANs," *Sci. China Inf. Sci.*, vol. 62, no. 10, Oct. 2019.
[7] C. Hu, Y. Li, X. Dong, and T. Long, "Optimal data acquisition and height retrieval in repeat-track geosynchronous SAR interferometry," *Remote Sens.*, vol. 7, no. 10, pp. 13367–13389, Oct. 2015.
[8] C. Hu, Y. Li, X. Dong, R. Wang, C. Cui, and B. Zhang, "Three-dimensional deformation retrieval in geosynchronous SAR by multiple-aperture interferometry processing: Theory and performance analysis," *IEEE Trans. Geosci. Remote Sens.*, vol. 55, no. 11, pp. 6150–6169, Nov. 2017.
[9] H. Yu, H. Lee, N. Cao, and Y. Lan, "Optimal baseline design for multibaseline InSAR phase unwrapping," *IEEE Trans. Geosci. Remote Sens.*, vol. 57, no. 8, pp. 5738–5750, Aug. 2019.
[10] V. Pascazio and G. Schirinzi, "Multifrequency InSAR height reconstruction through maximum likelihood estimation of local planes parameters," *IEEE Trans. Image Process.*, vol. 11, no. 12, pp. 1478–1489, Dec. 2002.
[11] G. Gomba, A. Parizzi, F. De Zan, M. Eineder, and R. Bamler, "Toward operational compensation of ionospheric effects in SAR interferograms: The split-spectrum method," *IEEE Trans. Geosci. Remote Sens.*, vol. 54, no. 3, pp. 1446–1461, Mar. 2016.
[12] D. P. S. Bekaert, "Statistical comparison of InSAR tropospheric correction techniques," *Remote Sens. Environ.*, vol. 170, pp. 40–47, Dec. 2015.